Layer-dependent anisotropic structural evolution in 1T'-ReSe$_2$: Pressure-induced phonon dynamics

Yuting Yan (严雨婷),[1] Liyuan Chen (陈丽媛),[1] Zian Hong (洪子安),[1] Kai Dai (戴凯),[1] Yafang Li (李亚芳),[1]
Kai Jiang (姜凯),[1,2,*] Ziyou Zhang (张自由),[3] Hongliang Dong (董洪亮),[3,4]
Liyan Shang (商丽燕),[1] and Zhigao Hu (胡志高)[1,5,†]
[1]*Technical Center for Multifunctional Magneto-Optical Spectroscopy (Shanghai), Engineering Research Center of Nanophotonics & Advanced Instrument (Ministry of Education), Department of Physics, School of Physics and Electronic Science, East China Normal University, Shanghai 200241, China*
[2]*School of Arts and Sciences, Shanghai Dianji University, Shanghai 201306, China*
[3]*Center for High Pressure Science and Technology Advanced Research, Shanghai 201203, China*
[4]*Shanghai Key Laboratory of Material Frontiers Research in Extreme Environments (MFree), Shanghai Advanced Research in Physical Sciences (SHARPS), Shanghai 201203, China*
[5]*Collaborative Innovation Center of Extreme Optics, Shanxi University, Taiyuan, Shanxi 030006, China*

(Received 21 June 2024; revised 30 March 2025; accepted 29 April 2025; published 12 May 2025)

Rhenium diselenide (ReSe$_2$) presents pronounced lattice anisotropy and relatively weak interlayer interactions, which can result in its superior compressibility under pressure, as compared to other two-dimensional (2D) transition metal dichalcogenides (TMDs). Here, we employed diamond anvil cells (DAC) to apply stress fields up to 15.90 GPa, unveiling the intricate relationships among layer numbers, anisotropic properties, and specific structural variations in ReSe$_2$. A rapid decrease in the anisotropic parameter σ from the E_g-like modes can be observed at 6–8 GPa. It was found that the layers (3, 10, and 17 L) could be correlated with the ratio of the *ab*-plane to *c*-axis components (I_{ab}/I_c), ultimately identifying the anisotropic structural deformation as either hydrostatic strain or uniaxial strain. Moreover, the pressure-dependent band gap analysis elucidated the interlayer interactions along the *c* axis. The present findings deepen understanding of ReSe$_2$'s structural response to stress field and facilitating advancements in strain-based device applications.

DOI: 10.1103/PhysRevB.111.195303

I. INTRODUCTION

Two-dimensional (2D) layered transition metal dichalcogenides (TMDs) represent a prominent subclass of layered materials renowned for their fascinating electrical, optical, and mechanical properties, attracting extensive research interest [1–3]. In recent years, Re-based compound ReSe$_2$ characterized by its unique in-plane anisotropy has emerged as a notable member within the class of 2D TMDs [4–7]. Due to the extremely weak interlayer coupling in ReSe$_2$, even bulk ReSe$_2$ behaves as electronically and vibrationally decoupled monolayers, the structural and performance differences among different layers of ReSe$_2$ are relatively minimal [8,9]. Upon applying external hydrostatic pressure to diminish interlayer distance and reinforce interlayer interactions, the discernible variations arising from alterations in the layer number will become more conspicuous. As an emerging external field modulation method, the pressure environment can exert influence on crystal structures by altering chemical bonds and interlayer coupling, and has been applied to enhance device performance, such as carrier mobility and interband transition [10–17]. Indeed, we previously observed that monolayer and bulk ReSe$_2$ exhibit distinct phase transition points derived from pressure-dependent spectral experiments, with monolayer ReSe$_2$ transition at 7.50 GPa and bulk at 8.94 GPa, respectively [11]. Under the influence of the stress field, ReSe$_2$ undergoes interlayer compression along the stacking direction (*c* axis) and overall lattice contraction.

Generally, the 1T′-ReSe$_2$ with space group $P\bar{1}$ exhibits covalent bonds between transition metal atoms (Re-Re), presenting a distorted trigonal structure (1T′) with its three principal axes nonperpendicular [18–20]. It possesses lower symmetry and pronounced in-plane anisotropy, with Re chains aligned along the b[010] axis, forming an angle of $\gamma = 118.89^\circ$ with the a[100] axis intersecting the *b* axis [21–23]. Experimentally, polarized Raman spectroscopy can effectively reflect the internal structure, chemical composition, and phonon mode properties, with the polarization module being particularly adept at analyzing lattice orientations [19,24]. By comparing the angle of maximum intensity ($I_{\max}$) of E_g-like and A_g-like mode across all θ values, the orientation of Re chains in the diamond anvil cell (DAC) can be ascertained. ReSe$_2$ can manifest either predominant uniaxial strain along the *z* axis of the laboratory coordinate system or isotropic hydrostatic strain, contingent upon the main stress components in *ab* plane or *c* axis [25]. The rotation angles of the Raman vibrational mode ($\Delta\theta_{1-4}$) between each pressure point and the vector components $|\overrightarrow{a}|$ and $|\overrightarrow{b}|$ reflect the variation in the vector distribution of E_g-like and A_g-like modes within the *ab*-plane. By systematically examining the in-plane

---

[*] Contact author: 32077@sdju.edu.cn

[†] Contact author: zghu@ee.ecnu.edu.cn

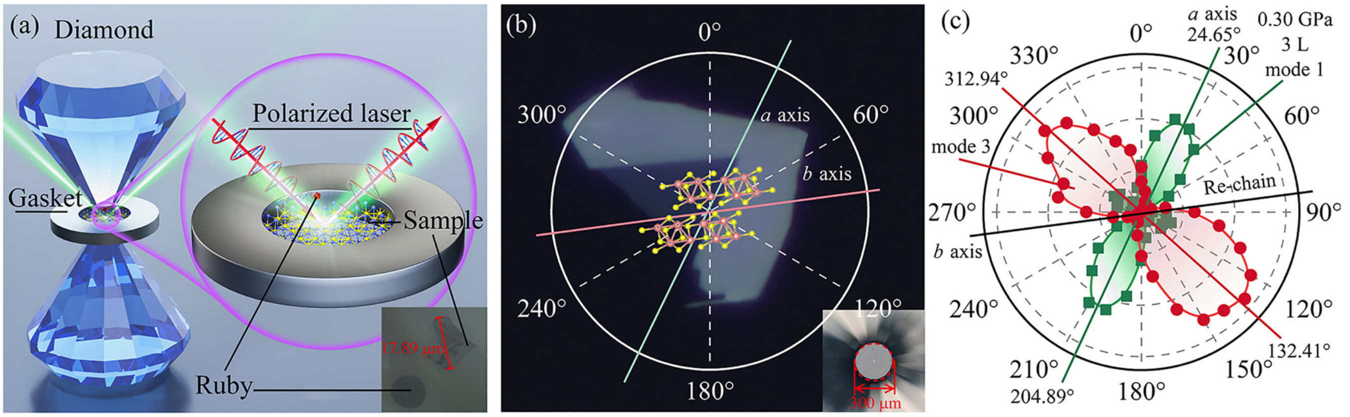

FIG. 1. Schematic illustration of the high pressure condition generated by the diamond anvil cell (DAC) and the determination of the crystallographic axis orientation. (a) The overall internal structure of DAC. A polarized laser was irradiated onto the sample. The sample and ruby transferred onto the diamond using a transfer stage, with silicone oil fully filling the entire chamber are shown in the inset figure. (b) The thin layer $ReSe_2$ obtained through mechanical exfoliation, along with the crystallographic axis orientation determined by polarized Raman spectroscopy. The inset figure shows a diamond anvil with a diameter of 300 μm. (c) The angular dependence of phonon modes 1 (E_g-like mode) and mode 3 (A_g-like mode) of 3 L $ReSe_2$ under 0.30 GPa, as obtained from polarized Raman spectroscopy. The directions of the Re chains (*b* axis) and the *a* axis have been determined.

and out-of-plane phonon modes $\Delta\theta_{1-4}$ and the anisotropy parameter σ, the vectorial evolution of phonon modes, and structural phase transitions in $ReSe_2$ under high pressure can be specifically investigated.

In this work, we systematically investigate the pressure effect on the structure and stress-induced deformation configurations of $ReSe_2$ with varying layer thicknesses (3, 10, and 17 L) through optical spectroscopy and phonon dispersion calculations. Despite the extensive research on high-pressure studies of 2D TMDs material systems, the $ReSe_2$ utilized in this work are few-layer films obtained through mechanical exfoliation, eliminating the influence of the substrate. The stress field imparted by diamond will directly act on $ReSe_2$. It was found that the dominant interlayer interaction along the *c* axis leads to stress-induced deformation in 3 L $ReSe_2$, transition to uniaxial strain along the *z* axis. In the case of the 17 L $ReSe_2$, the *ab*-plane vector component exhibits an increase compared to 3 L, resulting in a transition of the stress state towards hydrostatic and causing an increase in $\Delta\theta_1$. The findings provides insights into the physical structural properties of $ReSe_2$ under stress field, which could be helpful for optimizing the device performances.

II. RESULTS AND DISCUSSION

Generally, the $ReSe_2$ exhibits 18 Raman-active modes, represented by $\Gamma_{\text{Raman-active}} = 18A_g$, with the E_g-like and A_g-like modes serving as the primary characteristic phonon modes [4]. The vibration directions of in-plane and out-of-plane phonon modes on the *ab* plane are determined by deriving and fitting I_θ using experimental data for $\theta = 0°, 10°, 20°, \ldots, 350°$, and then fitting it with the first derivative to obtain the θ value at the maximum of I_θ. We employed this method to determine the crystal orientation of the $ReSe_2$ within the DAC (see in Fig. 1). Figure S1 present the characterization of few-layer $ReSe_2$ using pressure-dependent angle-dispersive x-ray diffraction (XRD) (Fig. S1 [26]). The (001) peak of thin layered $ReSe_2$ still persists under high pressure. The disappearance of the (002) peak is attributed to the compression of the interlayer spacing. Figure S2 presents the thickness and surface morphology information obtained via Atomic Force Microscopy (AFM) for 3, 10, and 17 L $ReSe_2$, respectively (Fig. S2 [26]). The specific layer numbers of the three samples were determined based on the thickness and PL band gap information. The Raman intensities exhibit an inverse relationship with the thickness. It can be seen that the 3 L $ReSe_2$ displays a higher intensity (Fig. S3 [26]). However, the structural information of $ReSe_2$ obtained solely from layer-dependent and pressure-dependent Raman spectroscopy remains insufficient. At this stage, polarized Raman spectroscopy (Fig. S4 [26]) was incorporated to conduct an in-depth analysis of structural evolution. As depicted in Fig. 2(a), it is evident that in-plane vibrations (E_g-like) and out-of-plane vibrations (A_g-like) have distinctly different anisotropic characteristics under parallel-polarized (VV) and crosspolarized (VH) configuration, respectively. In the ball-and-stick model viewed along the *a* axis, the E_g-like mode primarily exhibit vibrations perpendicular to the *c* axis, while the A_g-like mode has a significant component along the *c* axis. Figures 2(b) and 2(c) represent the vibration orientation of 4 Re and 8 Se atoms in *ab* and *ac* planes, respectively. The Re atoms in mode 1 manifest pronounced vibrations along the *a* axis, and the phonon vector direction of the Se atoms also aligns with the *a* axis. Mode 3 showcases the minimal displacements within the *ab* plane and maintain relative stability, as compared to the Re-chains. The intensities of Raman vibration modes involve a coupling of multiple variables, including layer thickness, pressure, polarization angle of incident light, and distinct phonon modes, are presented in Figs. 2(d)–2(g) and Figs. S5 and S6, respectively [26]. The anisotropic properties to a significant extent reflect the stability of its Re-chains and Re-Re bond structure, which can be quantified using the anisotropic parameter σ

$$\sigma = n'(I_{\max} - I_{\min}) \Big/ \sum I_{n'}, \qquad (1)$$

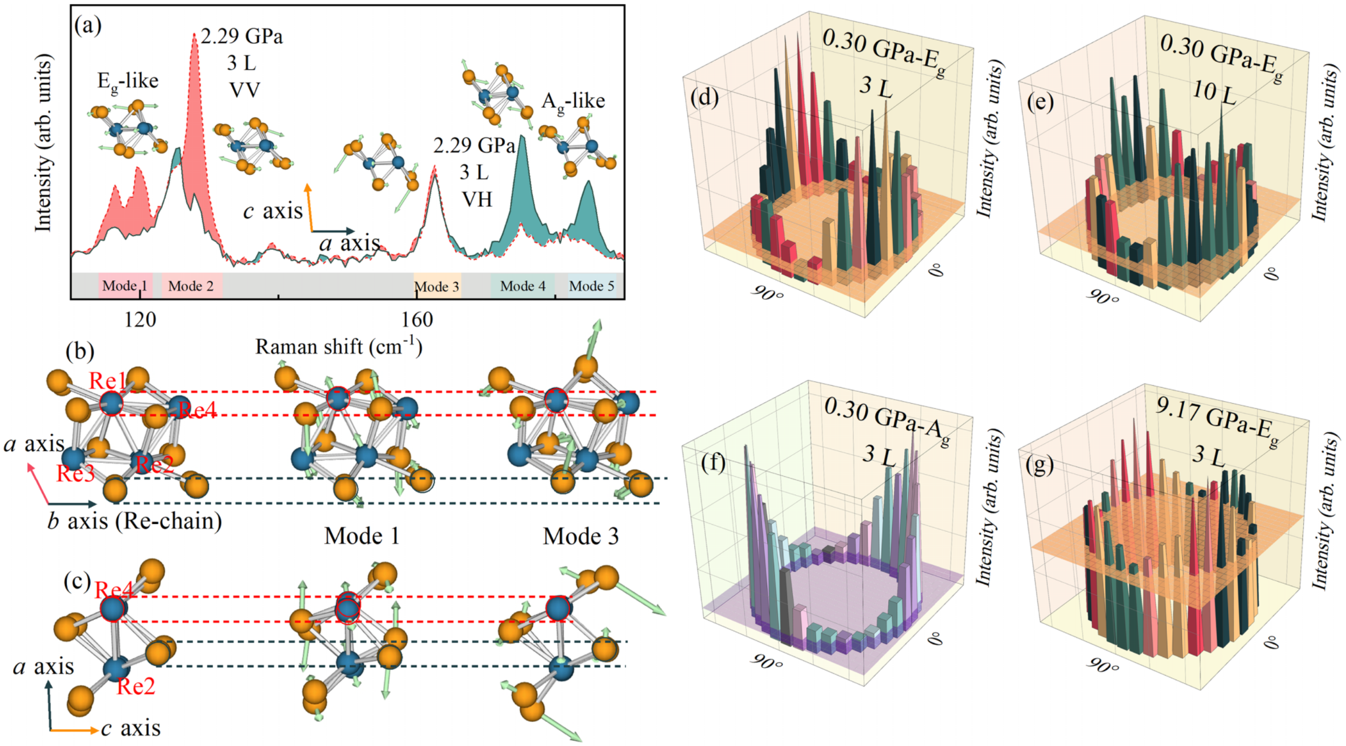

FIG. 2. Raman spectroscopy data and molecular structure evolution of $ReSe_2$. (a) Comparison of the VV (red) and VH (green) configuration Raman spectrum of 3 L $ReSe_2$ at 2.29 GPa. The ball-and-stick models illustrate the specific structural vibration directions of in-plane (modes 1 and 2) and out-of-plane vibrational modes (modes 3, 4, and 5). [(b) and (c)] The vibrational behaviors and atomic displacements of Re and Se atoms in the *ab* plane and *bc* plane of $ReSe_2$ with a unit cell. (d) Angle dependence of 3 L $ReSe_2$ E_g-like modes at 0.30 GPa in comparison with (e) E_g-like Raman modes of 10 L $ReSe_2$ at 0.30 GPa, (f) A_g-like Raman modes of 3 L $ReSe_2$ at 0.30 GPa, and (g) E_g-like Raman modes of 3 L $ReSe_2$ at 9.17 GPa. The orange or light purple planes indicate the planes where the minimum intensity ($I_{\min}$) occurs.

aiding in the analysis of the phonon configuration and structural evolution of $ReSe_2$. The variable n' represents the number of values used to calculate I, equals 36 when computed at intervals of 10° per point. Due to the crystalline structure of layered $ReSe_2$, which exhibits strong directional dependence, the anisotropy parameter σ quantifies the of anisotropy performance. A higher σ value indicates a greater anisotropy performance, while σ closer to 0 suggests that the material approaches isotropy.

By comparison in Table I, a decline in σ is observed owing to the interlayer van der Waals interactions induced by multilayer stacking with the increase in layers. Under the influence of the stress field, a rapid decrease of σ_{E_g} is observed at 6–8 GPa, which correlates with the structural phase transition identified in our previous studies [11]. At higher pressure points beyond 8 GPa, the anisotropy parameter of the A_g-like phonon mode is larger compared to the E_g-like mode. As shown in Table II, the magnitude of the vector components along the b and a axes can be expressed as

TABLE I. Calculated σ_{E_g} and σ_{A_g} values for Raman spectra experimental data obtained from samples of 3, 10, and 17 L $ReSe_2$ at various pressure points.

Pressure	Layer	σ_{E_g}	σ_{A_g}	Pressure	Layer	σ_{E_g}	σ_{A_g}
0–2 GPa	3 L	2.21	2.10	2–4 GPa	3 L	2.80	2.16
	10 L	1.84	1.74		10 L	2.09	1.81
	17 L	1.33	1.82		17 L	1.46	1.73
4–6 GPa	3 L	2.29	2.34	6–8 GPa	3 L	0.52	1.80
	10 L	1.43	1.78		10 L	0.72	1.67
	17 L	0.93	1.74		17 L	0.55	1.54
8–10 GPa	3 L	0.77	1.70	10–12 GPa	3 L	0.79	1.92
	10 L	0.47	1.52		10 L	0.42	1.20
	17 L	0.53	1.58		17 L	0.58	1.30

$$|b| = \sum_{n=1}^{12N} |b_n| = \sum_{n=1}^{12N} \left| \nu_{b_n} + \nu_{a_n} \cos\gamma + \nu_{c_n} \cos\alpha \right|,$$

$$|a| = \sum_{n=1}^{12N} |a_n| = \sum_{n=1}^{12N} \left| \nu_{a_n} + \nu_{b_n} \cos\gamma + \nu_{c_n} \cos\beta \right|, \quad (2)$$

for atom ordinal $n = 1, 2, 3, \ldots, 12N$, while N represents the number of layers. Substituting $\gamma = 118.89^\circ$, $\alpha = 104.38^\circ$ and $\beta = 91.86^\circ$ are based on the lattice constant. The angle φ_3 between mode 3 and the b axis is maintained around 52° during phonon dispersion calculations, which persists even after the phase transition pressure point. Due to the stability of mode 3 relative to the Re-chains, it can be obtained the vector distribution of other phonon modes by analyzing the angles between these modes and mode 3 in Raman experiments. The pressure-dependent angle variations of mode 1, mode 2 pertaining to the E_g-like mode, while mode 3 and mode 4 associated with the A_g-like mode, have been illustrated in Fig. 3. By fitting

TABLE II. The frequencies and the angle (φ) between the b axis of E_g-like and A_g-like modes were calculated through phonon dispersion calculations at 0, 3.76, 5.82, and 7.89 GPa, respectively.

Pressure	mode 1			mode 2			mode 3			mode 4		
	$\lvert\vec{a}\rvert$	$\lvert\vec{b}\rvert$	φ (°)	$\lvert\vec{a}\rvert$	$\lvert\vec{b}\rvert$	φ (°)	$\lvert\vec{a}\rvert$	$\lvert\vec{b}\rvert$	φ (°)	$\lvert\vec{a}\rvert$	$\lvert\vec{b}\rvert$	φ (°)
0 GPa	4.98	3.82	107.96	4.89	4.44	64.14	3.19	3.62	53.39	3.71	4.84	46.91
3.76 GPa	5.09	4.27	112.14	2.45	3.52	42.65	3.56	3.98	54.10	3.63	3.98	55.00
5.82 GPa	3.69	4.30	127.83	2.90	4.15	42.71	3.86	4.48	52.31	2.92	2.61	64.81
7.89 GPa	2.99	4.71	147.08	2.65	3.98	40.92	2.82	3.54	48.57	4.39	4.35	59.84

the relationship between Raman scattering intensity and angle θ at different pressure points, the specific angle values corresponding to the maximum intensity ($I_{\max}$) were recorded. We extracted the angle difference $\Delta\theta$ of mode 1-4 ($\Delta\theta_1$, $\Delta\theta_2$, $\Delta\theta_3$, $\Delta\theta_4$) between each pressure point. As shown in Fig. 3(a), the change of $\Delta\theta_1$ (31.91° to 52.77°) correlates positively with the increasing number of layers (3 L to 17 L) from ReSe$_2$, revealing the dependence of the a axis rotation angles on the layers. Due to the poor adhesion of thicker ReSe$_2$ (17 L) to the substrate, their in-plane compressibility is primarily determined by the ReSe$_2$'s own compressibility, resulting in a significantly higher in-plane compressibility compared to the 3 L case. The pressure exerted by the diamond is equivalent to hydrostatic pressure, characterized by a uniform stress distribution along the x, y, and z directions in the laboratory coordinate axes. In an ideal condition, $|\vec{F_x}| = |\vec{F_y}| = |\vec{F_z}| = \frac{\sqrt{3}}{3}|\vec{F}|$. The compressibility of ReSe$_2$ along the z axis exhibits a significant reduction with decreasing the layers. The stress components previously balanced along the x, y, and z axes exert stronger repulsive forces along the z axis due to the decreased interlayer distance, leading to an increase for $|\vec{F_z}|$. Meanwhile, atomically thin samples such as 3 L ReSe$_2$, typically exhibit strong adhesion to the substrate, thereby making their in-plane compressibility primarily governed by the in-plane compressibility of the diamond [27,28]. Under nonhydrostatic conditions, wrinkling or delamination phenomena may arise from the in-plane compressibility mismatch between a material and its substrate [29]. ReSe$_2$ belongs to TMDs, whose linear bulk modulus is significantly lower than that of diamond [30], necessitating consideration of wrinkling or delamination in few-layer ReSe$_2$ under compression. However, PTM-material interactions modulate adhesion energy and bending rigidity, thereby influencing wrinkle dynamics. In our experiments, the hydrostatic limit of the chosen PTM (silicone oil) exceeds our maximum pressure range, and its low chemical reactivity likely reduces interfacial infiltration compared to alcohols. Consequently, the influence of ReSe$_2$ wrinkling or delamination can be disregarded in the analysis of few-layer ReSe$_2$. The initial equilibrium of hydrostatic pressure shifts towards uniaxial strain along the z axis. Due to the misalignment between the c axis direction of the sample and the z axis of the laboratory coordinate system, it is necessary to calculate the component of $|\vec{F_z}|$ along the c axis. After substituting the lattice parameters (note S7 [26]), the angle ϕ_c between c axis and z axis can be obtained as 17.71°, while the ab-plane component $I_{ab} = |\vec{F_z}|\ \tan\varphi_c = 0.32|\vec{F_z}| = 0.30\ I_c$. The majority of the stress induced by uniaxial strain along the c axis is dissipated through interlayer interactions and inter-

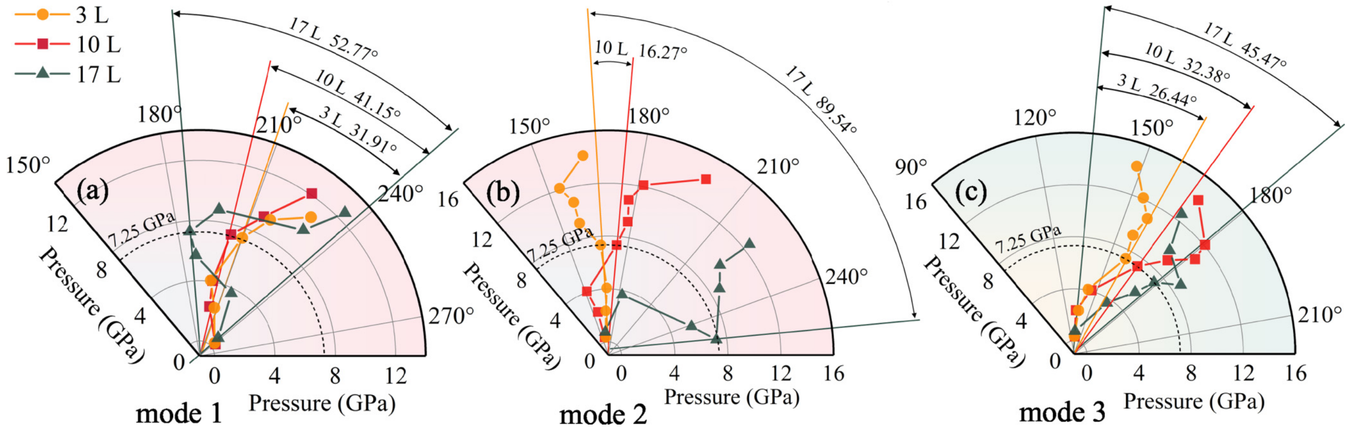

FIG. 3. The dependency of the angle (θ) corresponding to the fixed maximum Raman intensity ($I_{\max}$) of different phonon modes on pressure. The angles rotated clockwise or counterclockwise with increasing pressure are recorded as $\Delta\theta$. (a) Angular difference of mode 1 ($\Delta\theta_1$), (b) mode 2 ($\Delta\theta_2$), (c) mode 3 ($\Delta\theta_3$) of 3, 10, and 17 L ReSe$_2$, respectively. The dashed lines represent the inferred phase transition pressure point at 7.25 GPa.

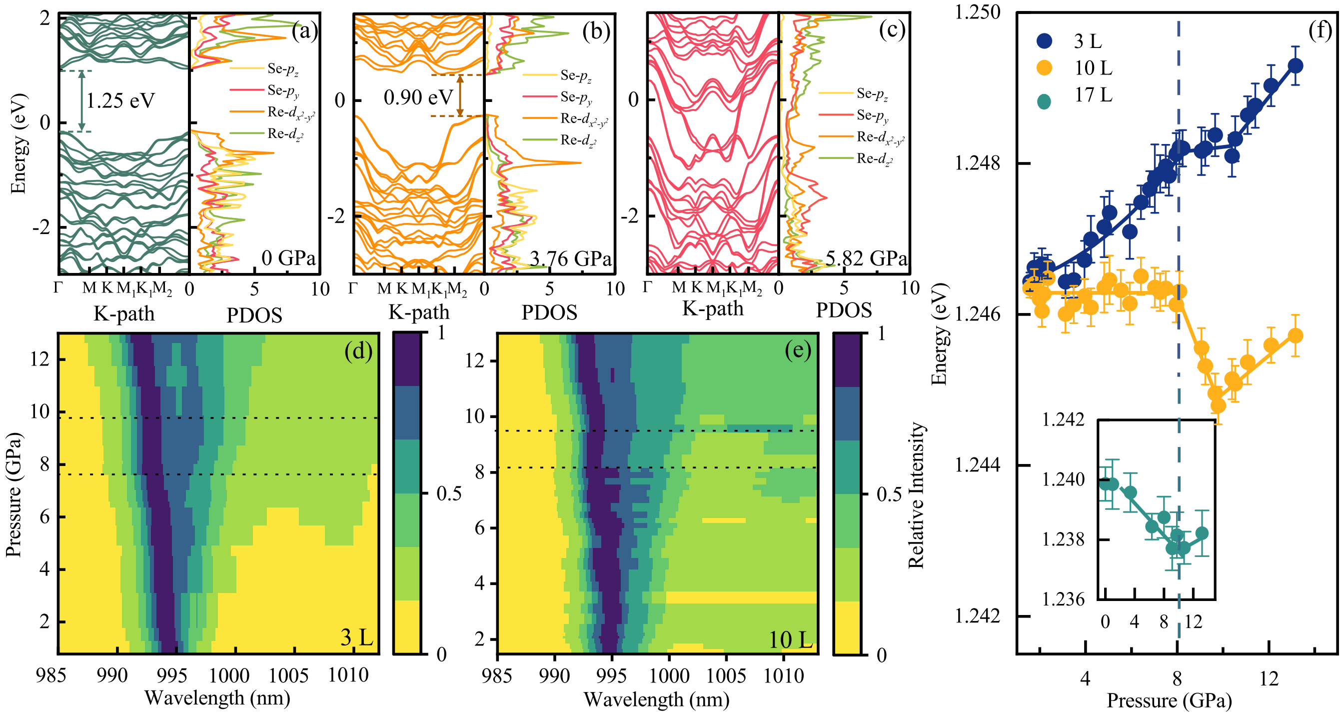

FIG. 4. The DFT-calculated band structures and the projected density of states (PDOS) of bilayer $ReSe_2$ at (a) 0, (b) 3.77, and (c) 5.82 GPa, respectively. Projections of Re and Se atoms on different orbitals are presented. [(d)–(e)] Measured photoluminescence spectra and pressure dependent diagram of 3 L and 10 L $ReSe_2$. The relationship between color and intensity of the blocks is shown by the scale on the right. The dashed line represents pressure points where significant variations in photoluminescence spectra trends occur. (f) Representative pressure-dependent relative photoluminescence spectra of 3, 10, and 17 L $ReSe_2$, respectively.

layer sliding forces. Nevertheless, under the ideal hydrostatic pressure environment, there are the following formula:

$$|\vec{a}| = \left||\vec{F_x}|\cos\left(\gamma - \frac{\pi}{2}\right)\right| + ||\vec{F_y}|\cos\gamma| + ||\vec{F_z}|\tan\phi_c\cos\beta|, \quad (3)$$

$$|\vec{b}| = |\vec{F_y}| + ||\vec{F_z}|\tan\phi_c\cos\alpha|, \quad (4)$$

$$|\vec{F_x}| = |\vec{F_y}| = |\vec{F_z}| = \frac{\sqrt{3}}{3}|\vec{F}|. \quad (5)$$

The vector magnitudes are determined to be $|\vec{a}| = 0.79|\vec{F}|$ and $|\vec{b}| = 0.62|\vec{F}|$, respectively. Through the equation in note S7, it is obtained that $I_{ab} = 0.73|\vec{F}| = 1.20 I_c$ [26].

The vibrational vector of mode 2 displays a less component along the z axis, with the ratio $I_{ab}/I_c = 2.61$. Hence, mode 2 exhibits a low I_c value and a significant contribution of interlayer interactions to the c axis component, enabling the neglect of in-plane c-axis deformation. The pressure-dependent variation of $\Delta\theta_2$ between 0.30 and 7.25 GPa for the 3 L $ReSe_2$ is only 3.52° from Fig. 3(b). The 17 L $ReSe_2$ exhibits a remarkably high $\Delta\theta_2$ value of 89.54°, primarily attributed to the quasi-hydrostatic pressure distribution arising from the increased layers, which aligns vibration vectors predominantly along the *ab*-plane. In the phonon dispersion calculations, we set and applied stress under the condition of absolute hydrostatic pressure, and obtained the value of $\Delta\theta_2$ as 23.22° (Table 2, Figs. S6 and S8 [26]). The $\Delta\theta_2$ for the 3 L and 10 L $ReSe_2$ (3.52° and 16.27°) in the pressure-dependent experiment are both smaller than 23.22°. Under uniaxial strain condition, in-plane distortion on the *ab*-plane weakens, as compared to hydrostatic conditions, resulting in a smaller $\Delta\theta_2$ than that predicted by phonon dispersion calculations based on absolute hydrostatic pressure. Therefore, the 3 and 10 L $ReSe_2$ can be considered to be subjected to uniaxial strain, whereas the 17 L $ReSe_2$ can be interpreted as experiencing a hydrostatic strain. The Re-Re bonds formed by Re1 and Re2 atoms exhibit a 52.77° counterclockwise rotation relative to the a axis in 17 L $ReSe_2$. Re3 and Re4 atoms elongate along the direction perpendicular to the a axis under uniaxial strain condition, while they experience significant distortion along the a axis under hydrostatic condition.

Herein, we conducted an analysis on two out-of-plane vibrational phonon modes and investigated their evolution with increasing the pressure. Mode 3 exhibits I_{ab}/I_c values of 1.01 [see Fig. 3(c)]. Due to the contribution of I_c, characterization of structural information in the Raman spectra related to out-of-plane vibrational modes necessitates consideration of the component along the c axis. Consequently, we investigated the interlayer compression at different layer numbers using PL spectra. As represented in Figs. 4(a)–4(c), the Density functional theory (DFT) calculated band structures and the projected density of states (PDOS) of $ReSe_2$ under different pressure points reveals pressure-induced band gap modifications and projections of Re-d and Se-p orbitals. The orbital projections at the conduction band minimum (CBM) are predominantly from Re-d_{z^2}, while those at the valence band maximum (VBM) are mainly from Re-$d_{x^2-y^2}$

and Se-p_z orbitals. Notably, the energy difference between Re-d_{z^2} and Se-p_z orbitals across the CBM and VBM stands out as the most pronounced among all orbital contributions [31]. The d_{z^2} component on the CBM exceeds that on the VBM, hence as the number of layers decreases and $ReSe_2$ experiences compression tending towards uniaxial strain, the disparity between the CBM and VBM intensifies. The measured pressure-dependent PL spectra of 3 and 10 L $ReSe_2$ are displayed in Figs. 4(d) and 4(e). Upon extracting the precise band gap values, it has been observed that a widening band gap in 3 L $ReSe_2$ [Fig. 4(f)], confirming the theoretical prediction of an increased CBM-VBM energy difference under uniaxial strain. In the case of 17 L $ReSe_2$, it is observed that as the pressure increases, the band gap undergoes an initial contraction. The narrowing of the band gap in $ReSe_2$ is primarily attributed to its unique crystal structure and the special electronic configuration of Re, which endows $ReSe_2$ with properties exhibiting negative pressure coefficients. Following the pressure exceeding the phase transition point, material structural alterations induce an overlap of electronic clouds, consequently causing the expansion of the band gap.

III. CONCLUSION

In summary, we introduce a new dimension to analyze the structural compression and torsion of $ReSe_2$ at different thickness, providing a method to identify the type of exerted strain and specific structural changes actually acting on $ReSe_2$. The pressure effect on physical structural variation, anisotropic performance and band gap transition of 3, 10, 17 L $ReSe_2$ have been systematically investigated. The number of layers dictates the distribution of stress vectors for $ReSe_2$ both on the *ab* plane and along the *c* axis, ultimately determining the specific deformation configuration under stress field. Especially, the 3 L $ReSe_2$ demonstrates enhanced interlayer interactions and a predisposition towards uniaxial strain, accompanied by an anomalous widening of the band gap with increasing pressure. As the thickness of $ReSe_2$ increases, the rising $\Delta\theta$ indicates an enhanced *ab*-plane component, resulting in a gradual transition towards standard hydrostatic strain under pressure. These findings of in-plane compression and interlayer interactions provide valuable insights into the pressure-induced structural deformation and band gap variation in 2D TMDs.

ACKNOWLEDGMENTS

This work is financially supported by the National Natural Science Foundation of China (Grants No. 62090013, and No. 62375086), the Projects of Science and Technology Commission of Shanghai Municipality (Grant No. 21JC1402100), and the Program for Professor of Special Appointment (Eastern Scholar) at Shanghai Institutions of Higher Learning.

APPENDIX A: SAMPLE PREPARATION

The 1T′-$ReSe_2$ was grown in a three-zone horizontal tube furnace with the chemical vapor transport (CVT) method. Re_2O_7 and Se particles were homogeneously blended in stoichiometric ratios and encapsulated in an ampule. The mixture was then subjected to annealing at 800 °C for 72 hours to synthesize $ReSe_2$. Subsequently, a predetermined amount of $ReSe_2$ along with a transport agent was enclosed in a 30 cm quartz tube. Crystal growth was facilitated using the CVT method for a duration of 300 hours, with heating temperatures maintained at 1000 °C and 550 °C at the hot and growth ends, respectively. $ReSe_2$ thin films with three different layers were obtained using mechanical exfoliation.

APPENDIX B: HIGH-PRESSURE XRD, RAMAN SCATTERING MEASUREMENTS AND CONSTRUCTION

In situ high-pressure angle-dispersive x-ray diffraction (XRD) experiments at the BL15U1 beamline of the Shanghai Synchrotron Radiation Facility (SSRF) with a wavelength of 0.6199 Å were conducted. Calibration was performed using CeO_2 as the standard sample. Subsequently, XRD data were collected using an imaging plate detector and processed using the DIOPTAS software to generate one-dimensional XRD patterns. The surface morphology of $ReSe_2$ is detected by atomic force microscopy (AFM, Dimension Icon, Brucker).

Raman scattering measurements were conducted employing a Jobin-Yvon LabRAM HR Evolution spectrometer. Excitation was provided by a laser with a wavelength of 532 nm, coupled with a 1800 grooves/mm grating. Laser focusing was achieved using a 50×objective. The experimental setup involved positioning the polarizer and analyzer in the excitation and detection paths, respectively. A rotatable half-wave plate, featuring a phase retardation of $\lambda/2$, was situated above the objective to modulate the angle of the incident light. The rotation of the half-wave plate facilitated the acquisition of data regarding the sample's characteristics at different angular orientations. A Mao-Bell-type DAC, fitted with a stainless steel gasket and two 300 μm culet diamonds, was applied to create high-pressure environment. Silicone oil was used as a pressure transfer medium (PTM). The pressure value was calibrated by ruby luminescence method.

APPENDIX C: DFT CALCULATION METHODS

The density functional theory (DFT) calculations employing the projector augmented wave (PAW) method were performed within the Vienna *ab initio* simulation package (VASP) to describe ion-electron interactions. The Perdew-Burke-Erzerhof (PBE) generalized gradient approximation (GGA) was employed to approximate the exchange-correlation functional. The 1T′-phase structure was modeled using a unit cell containing four formula units. Energies are reported in units of eV/f.u. Structural optimization convergence thresholds were set to $1.0\times1\times10^{-6}$ for energy and 0.01 eV/Å for force. A 15×15×1 Monkhorst-Pack *k*-point mesh was employed to sample the Brillouin zone. The harmonic approximation within the PHONOPY package was used to calculate the vibrational energy and entropy. Fully optimized geometries were used to calculate vibrational frequencies based on their force constant matrix.

[1] Y. Zhou, J. Sung, E. Brutschea, I. Esterlis, Y. Wang, G. Scuri, R. J. Gelly, H. Heo, T. Taniguchi, K. Watanabe, G. Zarand, M. D. Lukin, P. Kim, E. Demler, and H. Park, Bilayer Wigner crystals in a transition metal dichalcogenide heterostructure, Nature (London) **595**, 48 (2021).

[2] Q. Dong, J. Pan, S. J. Li, Y. Q. Fang, T. Lin, S. Liu, B. Liu, Q. Y. Li, F. Q. Huang, and B. B. Liu, Record-High superconductivity in transition metal dichalcogenides emerged in compressed 2H-TaS_2, Adv. Mater. **34**, 2103168 (2022).

[3] B. B. Yue, W. Zhong, X. H. Yu, and F. Hong, Superconductivity in the van der Waals crystal SnS_2 up to 105 GPa, Phys. Rev. B **105**, 104514 (2022).

[4] Y. Choi, K. Kim, S. Y. Lim, J. Kim, J. M. Park, J. H. Kim, Z. Lee, and H. Cheong, Complete determination of the crystallographic orientation of ReX_2 (X=S, Se) by polarized Raman spectroscopy, Nanoscale Horiz. **5**, 308 (2020).

[5] M. Hafeez, L. Gan, H. Q. Li, Y. Ma, and T. Y. Zhai, Chemical vapor deposition synthesis of ultrathin hexagonal $ReSe_2$ flakes for anisotropic Raman property and optoelectronic application, Adv. Mater. **28**, 8296 (2016).

[6] L. Kipczak, M. Grzeszczyk, K. Olkowska-Pucko, A. Babiński, and M. R. Molas, The optical signature of few-layer $ReSe_2$, J. Appl. Phys. **128**, 044302 (2020).

[7] F. F. Cui, X. B. Li, Q. L. Feng, J. B. Yin, L. Zhou, D. Y. Liu, K. Q. Liu, X. X. He, X. Liang, S. Z. Liu, Z. B. Lei, Z. H. Liu, H. L. Peng, J. Zhang, J. Kong, and H. Xu, Epitaxial growth of large-area and highly crystalline anisotropic $ReSe_2$ atomic layer, Nano Res. **10**, 2732 (2017).

[8] S. Tongay, H. Sahin, C. Ko, A. Luce, W. Fan, K. Liu, J. Zhou, Y. S. Huang, C. H. Ho, J. Yan, D. F. Ogletree, S. Aloni, J. Ji, S. Li, J. Li, F. M. Peeters, and J. Wu, Monolayer behaviour in bulk ReS_2 due to electronic and vibrational decoupling, Nat. Commun. **5**, 3252 (2014).

[9] M. Hong, X. B. Zhou, N. Gao, S. L. Jiang, C. Y. Xie, L. Y. Zhao, Y. Gao, Z. P. Zhang, P. F. Yang, Y. P. Shi, Q. Zhang, Z. F. Liu, J. J. Zhao, and Y. F. Zhang, Identifying the non-identical outermost selenium atoms and invariable band gaps across the grain boundary of anisotropic rhenium diselenide, ACS Nano **12**, 10095 (2018).

[10] Z. Zhou, J.-J. Zhang, G. F. Turner, S. A. Moggach, Y. Lekina, S. Morris, S. Wang, Y. Q. Hu, Q. K. Li, J. S. Xue, Z. J. Feng, Q. Y. Yan, Y. Y. Weng, B. Xu, Y. Fang, Z. X. Shen, L. Fang, S. Dong, and L. You, Sliding-mediated ferroelectric phase transition in $CuInP_2S_6$ under pressure, Appl. Phys. Rev. **11**, 011414 (2024).

[11] Y. T. Yan, L. Y. Chen, K. Dai, Y. F. Li, L. Wang, K. Jiang, A. Y. Cui, J. Z. Zhang, and Z. G. Hu, Anisotropic phonon behavior and phase transition in monolayer $ReSe_2$ discovered by high pressure Raman scattering, J. Phys. Chem. Lett. **14**, 7618 (2023).

[12] X. D. Yao, Y. X. Bai, C. Jin, X. Y. Zhang, Q. F. Zheng, Z. D. Xu, L. Chen, S. M. Wang, Y. Liu, J. L. Wang, and J. L. Zhu, Anomalous polarization enhancement in a van der Waals ferroelectric material under pressure, Nat. Commun. **14**, 4301 (2023).

[13] L. G. P. Martins, R. Comin, M. J. S. Matos, M. S. C. Mazzoni, B. R. A. Neves, and M. Yankowitz, High-pressure studies of atomically thin van der Waals materials, Appl. Phys. Rev. **10**, 011313 (2023).

[14] S. Y. Huang, Y. Lu, F. J. Wang, Y. C. Lei, C. Y. Song, J. S. Zhang, Q. X. Xing, C. Wang, Y. G. Xie, L. Mu, G. W. Zhang, H. Yan, B. Chen, and H. G. Yan, Layer-dependent pressure effect on the electronic structure of 2D black phosphorus, Phys. Rev. Lett. **127**, 186401 (2021).

[15] A. P. Nayak, T. Pandey, D. Voiry, J. Liu, S. T. Moran, A. Sharma, C. Tan, C. H. Chen, L. J. Li, M. Chhowalla, J. F. Lin, A. K. Singh, and D. Akinwande, Pressure-dependent optical and vibrational properties of monolayer molybdenum disulfide, Nano Lett. **15**, 346 (2015).

[16] J. Ying, H. Paudyal, C. Heil, X.-J. Chen, V. V. Struzhkin, and E. R. Margine, Unusual pressure-induced periodic lattice distortion in $SnSe_2$, Phys. Rev. Lett. **121**, 027003 (2018).

[17] B. Szentpéteri, P. Rickhaus, F. K. de Vries, A. Márffy, B. F ülöp, E. Tóvári, K. Watanabe, T. Taniguchi, A. Kormányos, S. Csonka, and P. Makk, Tailoring the band structure of twisted double bilayer graphene with pressure, Nano Lett. **21**, 8777 (2021).

[18] D. Wolverson, S. Crampin, A. S. Kazemi, A. Ilie, and S. J. Bending, Raman spectra of monolayer, few-layer, and bulk $ReSe_2$: An anisotropic layered semiconductor, ACS Nano **8**, 11154 (2014).

[19] E. Lorchat, G. Froehlicher, and S. Berciaud, Splitting of interlayer shear modes and photon energy dependent anisotropic Raman response in N-layer $ReSe_2$ and ReS_2, ACS Nano **10**, 2752 (2016).

[20] Q. Tang, Tuning the phase stability of Mo-based TMD monolayers through coupled vacancy defects and lattice strain, J. Mater. Chem. C **6**, 9561 (2018).

[21] Y. Wan, T. Hu, X. Y. Mao, J. Fu, K. Yuan, Y. Song, X. T. Gan, X. L. Xu, M. Z. Xue, X. Cheng, C. X. Huang, J. B. Yang, L. Dai, H. L. Zeng, and E. J. Kan, Room-temperature ferroelectricity in $1T'$-ReS_2 multilayers, Phys. Rev. Lett. **128**, 067601 (2022).

[22] J. Seo, Y. Kim, J. Lee, E. Son, M.-H. Jung, Y.-M. Kim, H. Y. Jeong, G. Lee, and H. Park, A single-atom vanadium-doped 2D semiconductor platform for attomolar-level molecular sensing, J. Mater. Chem. A **10**, 13298 (2022).

[23] J. Kim, K. Heo, D. H. Kang, C. Shin, S. Lee, H. Y. Yu, and J. H. Park, Rhenium diselenide ($ReSe_2$) near-infrared photodetector: performance enhancement by selective *p*-doping technique, Adv. Sci. **6**, 1901255 (2019).

[24] Y. F. Li, A. Y. Cui, K. Dai, Y. T. Yan, K. Jiang, L. Y. Shang, L. Q. Zhu, Y. W. Li, J. Z. Zhang, X. Lv, J. G. Wu, and Z. G. Hu, Deciphering the structural heterogeneity behaviors of (K, Na)NbO_3-based piezoelectric ceramics with multi-scale analyses, Acta Mater. **265**, 119612 (2024).

[25] L. Y. Zhao, Y. J. Jiang, C. Li, Y. Liang, Z. M. Wei, X. D. Wei, and Q. Zhang, Probing anisotropic deformation and near-infrared emission tuning in thin-layered InSe crystal under high pressure, Nano Lett. **23**, 3493 (2023).

[26] See Supplemental Material at http://link.aps.org/supplemental/10.1103/PhysRevB.111.195303 for the Pressure-dependent angle-dispersive X-ray diffraction (XRD); Atomic Force Microscopy (AFM) images of $ReSe_2$ with different layers along with thickness annotations; Pressure-dependent Raman phonon modes variation of $ReSe_2$ in different layers; Optical path flow diagram in pressure- and angle-dependent Raman measurements; Anisotropic Raman response of $ReSe_2$ at 0.30-0.69 GPa; Polarized Raman intensity of $ReSe_2$ at 8.77-9.17 GPa; Calculation of ϕ_c and I_{ab}; Calculated phonon dispersion in four selected pressures.

[27] D. Machon, C. Bousige, R. Alencar, A. Torres-Dias, F. Balima, J. Nicolle, G. de Sousa Pinheiro, A. G. Souza Filho, and A.

San-Miguel, Raman scattering studies of graphene under high pressure, J. Raman Spectrosc **49**, 121 (2018).

[28] C. Bousige, F. Balima, D. Machon, G. S. Pinheiro, A. Torres-Dias, J. Nicolle, D. Kalita, N. Bendiab, L. Marty, V. Bouchiat, G. Montagnac, A. G. Souza Filho, P. Poncharal, and A. San-Miguel, Biaxial strain transfer in supported graphene, Nano Lett. **17**, 21 (2017).

[29] I. R. Amaral, A. Forestier, A. Piednoir, R. Galafassi, C. Bousige, D. Machon, O. Pierre-Louis, R. S. Alencar, A. G. Souza Filho, and A. San-Miguel, Delamination of multilayer graphene stacks from its substrate through wrinkle formation under high pressures, Carbon **185**, 242 (2021).

[30] N. Bandaru, R. S. Kumar, D. Sneed, O. Tschauner, J. Baker, D. Antonio, S.-N. Luo, T. Hartmann, Y. S. Zhao, and R. Venkat, Effect of pressure and temperature on structural stability of MoS_2, J. Phys. Chem. C **118**, 3230 (2014).

[31] R. Oliva, M. Laurien, F. Dybala, J. Kopaczek, Y. Qin, S. Tongay, O. Rubel, and R. Kudrawiec, Pressure dependence of direct optical transitions in ReS_2 and $ReSe_2$, npj 2D Mater. Appl. **3**, 20 (2019).